Modelling cortical laminar connectivity in the macaque brain

Ittai Shamir [a] and Yaniv Assaf [a,b]

[a] Department of Neurobiology, Faculty of Life Sciences, Tel Aviv University, Tel Aviv, Israel

[b] Sagol School of Neuroscience, Tel Aviv University, Tel Aviv, Israel

Abstract

In 1991, Felleman and Van Essen published their seminal study regarding hierarchical processing in the primate cerebral cortex. Their work encompassed a widescale analysis of connections reported through tracing between 35 regions in the macaque visual cortex, extending from cortical regions to the laminar level. Since then, great strides have been made in the field of MRI neuroimaging of white matter connectivity, also known as connectomics, as well as grey matter laminar composition. In this work, we revisit laminar-level connectivity in the macaque brain using a whole-brain MRI-based approach. We use multi-modal ex-vivo MRI imaging of both white and grey matter, which are then integrated via our simple model of laminar connectivity. This model uses a granularity-based approach to define a set of rules that expands cortical connections to the laminar level. The resulting whole-brain network of macaque cortical laminar connectivity is then validated in the visual cortex by comparison to Felleman and Van Essen's 1991 results. By using an unbiased definition of the cortex that addresses its heterogenous laminar composition, we are able to explore a new avenue of connectomics on the laminar level.

Introduction

In 1991, Felleman and Van Essen published their influential study regarding hierarchical processing in the primate cerebral cortex (Felleman and Van Essen 1991). The study encompassed a widescale analysis of cortical connections in the macaque brain, which have been reported using histological tracing. The connections link 35 cortical regions in the macaque visual cortex, extending from the regional level to the laminar level. Since then, their work has propelled the study of the interconnectedness of the visual cortex and has become a significant milestone in the field of connectomics.

Over the past decade, great progress has been made in the field of MRI imaging of white matter connectivity, also known as connectomics (Van Essen et al. 2013, Setsompop et al. 2013). Since then, neuroimaging research of brain connectivity has focused on three principal types of connectivity:

a. Structural connectivity: represents the anatomical links, or fiber bundles, connecting different cortical regions. Structural connectivity can be measured using MRI DWI tractography.
b. Functional connectivity: represents time series correlation between different cortical regions. Functional connectivity can be measured using BOLD fMRI.
c. Effective connectivity: represents the influence one cortical region exerts over another. It is based on a network model of causal dynamics that best explains the functional signals (state-dependent), while being constrained by the anatomy of structural connectivity.

Currently, one of the major limitations of tractography lies in the lack of information regarding the laminar end points of white matter tracts inside the cortical grey matter (Jbabdi and Johansen-Berg 2011). In other words, the field of connectomics is currently limited by the biased definition of the cortex as a homogenous unit, focusing on transverse partitioning into regions and ignoring radial partitioning into laminar components. The integration of microstructural information regarding cortical properties and macrostructural connectomics could pose an exciting development in the field, by offering a multi-scale micro-level connectome (Johansen-Berg 2013).

In recent years, promising progress has also been made in the field of MRI imaging of the cortical laminar composition of the cortex (Barazany and Assaf 2012, Lifshits et al. 2018, Shamir et al. 2019). More specifically, the methodology (presented by Shamir et al. 2019) offers a framework for MRI-based quantification and visualization of the cortical laminar composition. By integrating the laminar structure derived from this framework into connectomics, not only we will be able to give a more detailed and unbiased representation of brain connectivity, but we will also open a new avenue to future prospects in the field of connectomics (see figure 1).

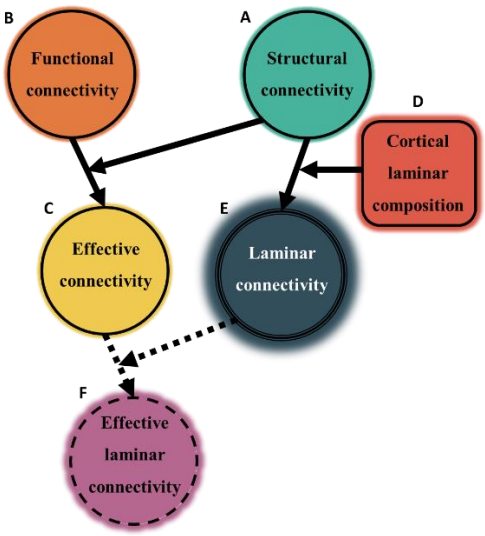

Fig. 1 The potential of cortical laminar composition in connectomics:
Integrating laminar composition (D) into structural connectivity (A) enables us to introduce laminar connectivity (E), similarly to the way in which integrating structural and functional (B) connectivity has led to effective connectivity (C). In the future, laminar and effective connectivity could conceivably be integrated into effective laminar connectivity (F)

In this study, we revisit Felleman and Van Essen's 1991 work and attempt to recreate it non-invasively, using MRI techniques to model and investigate the laminar connectivity of the macaque cerebral cortex. We do so while considering both the laminar organization as well as the interconnections of the cortex. We hypothesize that MRI, or more specifically diffusion weighted imaging (DWI), inversion recovery (IR) and T1w, can all be integrated into a whole-brain laminar connectome through a simple granularity-based model based on published histological findings (Shamir and Assaf 2020). The resulting whole-brain network of cortical laminar connectivity is then validated in the visual cortex by comparison to Felleman and Van Essen's 1991 results. By using an unbiased definition of the cortex that takes into account its heterogenous laminar composition, we are able to use MRI neuroimaging to explore laminar level connectomics.

Methods and materials

MRI Acquisition

MRI was performed on an excised macaque brain, on a 7T/30 Bruker scanner with a 660 mT/m gradient system. The protocol was approved by the Tel Aviv University ethics committee on animal research. Three MRI sequences were performed:

1. T1w sequence was performed with a 3D modified driven equilibrium Fourier transform (MDEFT) sequence with: voxel size 0.2×0.2×0.2 mm3, image size 300×360×220 voxels, TR/TE=1300/2.9 ms, TI=400 ms. This sequence was used as an anatomical reference with high gray/white matter contrast and used for segmentation and inner and outer surface estimation.
2. Inversion recovery was performed using a 3D FLASH sequence with: voxel size 0.67×0.67×0.67 mm3, image size 96×96×68 voxels, TR/TE=1300/4.672 ms and 44 inversion times spread between 25 ms up to 1,000 ms, each voxel fitted with up to 8 T1 values (similarly to Lifshits et al. 2018).
   T1w and inversion recovery datasets were used for cortical laminar composition analysis (similarly to the framework presented in Shamir et al. 2019).
3. DWI (diffusion weighted imaging) was performed with 4 segments diffusion weighted EPI sequence with a voxel size 0.48×0.48×0.48 mm3, image size 128×160×116 voxels, Δ/δ=20/3.3 ms, b=5000 s/mm2, with 96 gradient directions and additional 4 with b=0.
   DWI dataset was used for global white matter connectivity (tractography), using constrained spherical deconvolution (CSD) in ExploreDTI (Leemans et al. 2009).

Cortical atlas and template

1. Macaque cortical atlas (see Supplementary Material figure 1A): the FVE91 parcellation divides the cortex into 84 regions, as described by Daniel J. Felleman and David C. Van Essen (Felleman and Van Essen 1991).
2. Macaque cortical template (see Supplementary Material figure 1B): the F99 space is defined by a 0.5 mm MRI scan of an approximately 5-year-old male macaque monkey case F99UA1, provided by M. Logothetis and introduced by David C. Van Essen (Van Essen 2002).

Image registration

In the interest of transferring all datasets to a single anatomical space, all the following were registered to the MPRAGE image: T1 layer probability maps, DTI images, atlas and template. Registration was completed in SPM12 using a rigid body transformation with the first image of each dataset as the source image.

Image processing

1. Cortical volume sampling

In order to provide accurate volumetric sampling of the complex geometry of the cortex, we use the unique framework for cortical laminar composition analysis (presented by Shamir et al. 2019). The framework uses a sampling system made up of virtual cortical spheres, as a symmetric and rotationally invariant volumetric alternative to cortical normals.

1.1 Delineation of cortical surfaces

Since our subject is non-human, we offer a straightforward alternative to the human MPRAGE analysis and segmentation of the *FreeSurfer* pipeline (Fischl 2012). The alternative utilizes the registered FVE91 macaque cortical atlas to delineate each cortical surface, using the steps:

a. Outer cortical surface: delineating the border between cortical GM bordering and the surrounding CSF:
   1. Binarize the macaque cortical atlas
   2. Fill binarized atlas per cortical slice
   3. Rebuild entire filled hemispheric volumes from slices
   4. Split hemispheric volumes to left and right hemispheres
   5. Smooth both hemispheric volumes
   6. For each hemisphere, extract a triangular isosurface
   7. Resample each isosurface to ~150K vertices and ~300K faces
b. Inner cortical surface: delineating the border between cortical GM bordering and the underlying WM:
   1. Manually fill gaps in binarized cortical atlas (from step a. 1)
   2. Split cortical atlas to left and right hemispheres
   3. Per hemisphere, subtract cortical atlas (from step b. 2) from filled cortical volume (from step a.4)
   4. Smooth resulting binary images of hemispheric WM
   5. For each hemisphere, extract a triangular isosurface
   6. Resample each isosurface to ~150K vertices and ~300K faces
c. Mid cortical surface: estimating the center of cortical GM:
   Run through all vertices of inner surface (~150K per hemisphere), for each:
   1. Calculate normal direction to inner surface (cortical normal)
   2. Find closest vertex on outer surface and calculate minimal distance (cortical width at that point)
   3. Estimate location of corresponding mid surface vertex:
      Mid surface vertex=Inner surface vertex+0.5*minimal distance (in normal direction)

   Once all mid surface vertices have been estimated, reconstruct entire mid triangular surface (see Supplementary Material figure 2A).

1.2 Generation of spherical sampling system

Once all three cortical surfaces were delineated per hemisphere, our system of virtual cortical spheres was built, using mid surface vertices and half the value of their corresponding cortical thickness as sphere centers and radii (respectively). In order to avoid excessive volumetric overlap of cortical spheres (Shamir et al. 2019), we subsampled the mid surface vertices by a factor of 2, to ~75,000 spheres per hemisphere (see Supplementary Material figure 2B).

2. IR decay function fit

The IR EPI data were used for multiple T1 analysis, by calculating T1 values and their corresponding partial volumes on a voxel-by-voxel basis. The IR datasets were fitted to the conventional inversion recovery decay function with up to 8 possible T1 components per voxel (Lifshits et al. 2018):

$$\mathrm{M(TI_i)} = \sum_{j=1}^{7} \mathrm{M0_j} \cdot (1 - 2\mathrm{e}^{-\mathrm{TI_i}/\mathrm{T_{1j}}}) \quad (1)$$

Where:

$\mathrm{M(TI_i)}$- Magnetization at the ith inversion recovery image, in other words the magnetization measured for each specific T1 component.

$\mathrm{M0_j}$- Predicted magnetization at TI=0ms for each T1 component (j) in the voxel.

$\mathrm{T_{1j}}$- Longitudinal relaxation time for each T1 component.

j was set up to 7 for the low-resolution experiments, indicating fit to seven individual exponential fits, based on the assumption that there are 8 T1 components in the tissue – 1 for CSF, 1 for WM and heavily myelinated layer of the cortex and additional 5 cortical layers.

Normalization of each of the predicted magnetization values according to $\frac{\mathrm{M0_j}}{\sum_{\mathrm{i=1}}^{\mathrm{j}} \mathrm{M0_j}}$ then represents the voxel contribution of each corresponding T1 component (j).

3. T1 probabilistic classification

The multiple T1 components were used for accurate whole-brain classification to brain tissues on a voxel-by-voxel basis. A T1 histogram was initially plotted for this purpose. Each IR EPI set of images consists of up to ~5×10^6 potential T1 values: 96x96x68 [voxels] ×8 [T1 fitted values]. In order to represent all fitted T1 values according to their partial volumes in the histogram, each voxel was given a weight greater than one.

The T1 histogram was then fitted to a probabilistic mixture model (similarly to the method shown in Lifshits et al. 2018, Barazany et al. 2012, and Shamir et al. 2019), consisting of t-distributions (Peel et al. 2000, Shamir et al. 2019). The probability of each t-distribution in the voxel was calculated using Bayes' formula:

$$P_k = \sum_{i=1}^{8} f_i \cdot \frac{p(T_{1(i)}|k)p(k)}{p(T_{1(i)})} \quad (2)$$

Where:
k- A specific t-distribution.
$T_{1(i)}$- T1-value of the ith component of the voxel.
f_i- Partial volume of $T_{1(i)}$ (normalized as show in previous section).
$p(T_1)$- General whole-brain probability of a T_1-value.
$p(k)$- Probability of t-distribution k.
$p(T_1|k)$- Probability of the T_1-value in t-distribution k.

This model was used as a means of probabilistic classification of T1 values per subject into clusters. Selection of the appropriate number of t-distributions for the mixture model was completed using the Bayesian information criterion (BIC), a criterion used for probabilistic model selection. BIC uses a log likelihood function and penalizes for more complex models with additional parameters. The mixture model was fitted repeatedly using a different number of distributions each time, ranging between 1-20 distributions, and evaluated using –log of BIC value.

Fit to 11 t-distributions was deemed sufficient, where –log(BIC) reaches a maximal value with the fewest distributions. These 11 distinct T1 clusters correspond to different types of brain tissue (see Supplementary Material figure 3):

1. White matter (WM): characterized by low T1 values, represented by t-distributions 1-3.
2. Gray matter (GM): characterized by mid-range T1 values, represented by 4th-9th t-distributions corresponding to 6 T1 layers, with decreasing degrees of myelination. Because of the link between myelination and shorter T1 values, T1 layer 4 (4th t-distribution) represents the most highly myelinated and innermost cortical component, with decreasing degrees of myelination moving outwards up to the outermost cortical component- T1 layer 1 (9th t-distribution).
3. Cerebral spinal fluid (CSF): characterized by high T1 values, represented by t-distributions 10-11 (also includes signal noise).

4. Cortical volume sampling

One of the main challenges in implementing spherical sampling of low-resolution data lies in the resolution difference between the spherical sampling system (average radius of ~0.5 mm) and the T1 data ($0.67^3\ mm^3$). Overcoming this resolution gap demanded a super-resolution solution based on estimation of subvoxel information (similarly to Shamir et al. 2019). Our offered solution includes the following steps:

a. Partitioning each voxel into subvoxels:
Degree of partitioning was chosen so that each subvoxel has the largest volume while still enabling accurate group representation of a spherical volume with a radius of 1 mm. Consequently, each voxel was partitioned into 10^3 subvoxels, each assigned location properties, primarily its location inside or outside of a given sphere.

b. Assignment of spherical volume weights:
Each sphere in our sampling system was assigned weights, corresponding to each voxel's contribution to its spherical volume, according to the following equation:

$$W_{voxel_i,sphere_j} = \frac{N_{voxel_i,sphere_j}}{N_{sphere_j}} \quad (3)$$

Where:
$W_{voxel_i,sphere_j}$- Volume weight of voxel i per sphere j.
$N_{voxel_i,sphere_j}$- Number of subvoxels from voxel i located inside sphere j.
N_{sphere_j}- Total number of subvoxels located inside sphere j.

c. Cortical composition analysis inside sphere:
In order to estimate the cortical composition inside our sampling system, each sphere's volume weights were multiplied by their corresponding voxel's entire probabilistic content (see *T1 probabilistic classification*). In other words, the assignment of spherical weights does not make any assumptions regarding layer order. The process was repeated across all spheres in our entire sampling system, according to the following equation:

$$P(t_k/sphere) = \sum_{i=1}^{M} \sum_{k=2}^{7} W_{voxel_i,sphere_j} \cdot P(t_k/voxel_i) \quad (4)$$

Where:
$P(t_k/sphere)$- Probability of t-distribution k per sphere.

k- t-distributions 4,5,6,7, representing T1 layers 4,3,2,1 (respectively).
M- Number of voxels within which sphere j lies.
$W_{voxel_i,sphere_j}$- Volume weight of voxel i per sphere j.
$P(t_k/voxel_i)$- Probability of t-distribution k in voxel i.

5. DTI analysis and tractography

The DWI dataset was used for global white matter connectivity analysis. Constrained spherical deconvolution (Tournier 2007) was implemented for estimation of white matter fiber orientation distribution, using ExploreDTI (Leemans et al. 2009). The resulting whole-brain tractography was then analyzed for connectivity across FVE91 regions (see Supplementary Material figure 4).

6. Cortical granularity indices

An atlas of cortical granularity indices was formed based on a map of cytoarchitectonic features across the primate cortex (Beul and Hilgetag 2019). The chosen map features the variation in neuron density across M132 atlas regions of the macaque brain. The values, presented as the number of neurons per squared millimeter, were converted to a discrete scale of granularity indices, where higher ranges of neuron densities correlate to higher granularity indices (and vice versa). Missing values were interpolated using an average of the closest existing region values. Indices were then converted to the FVE91 atlas space, using the most common index (see figure 2).

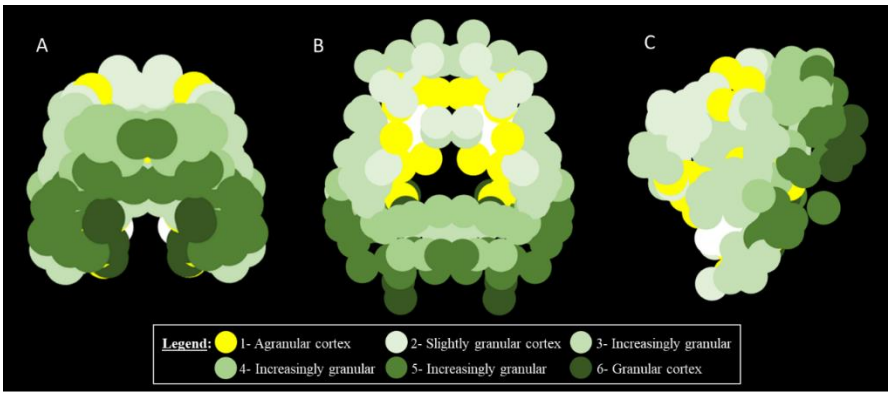

Fig. 2 Granularity indices across FVE91 atlas regions:
A- Occipital view; B- top view; C- left side view of left hemisphere

7. Modelling cortical layer connectivity

Datasets were integrated using an MRI-based, data-driven model of cortical laminar connectivity (similar to the one presented in Shamir and Assaf 2020). The model is based on a systematic review of a sample of articles focused on laminar connectivity, offering a way to overcome specificity and resolution limitations in MRI connectomics and presenting a simplified approach to integrating whole-brain white and grey matter MRI datasets into laminar-level connectivity (for a summary of the modelling framework see figure 3).

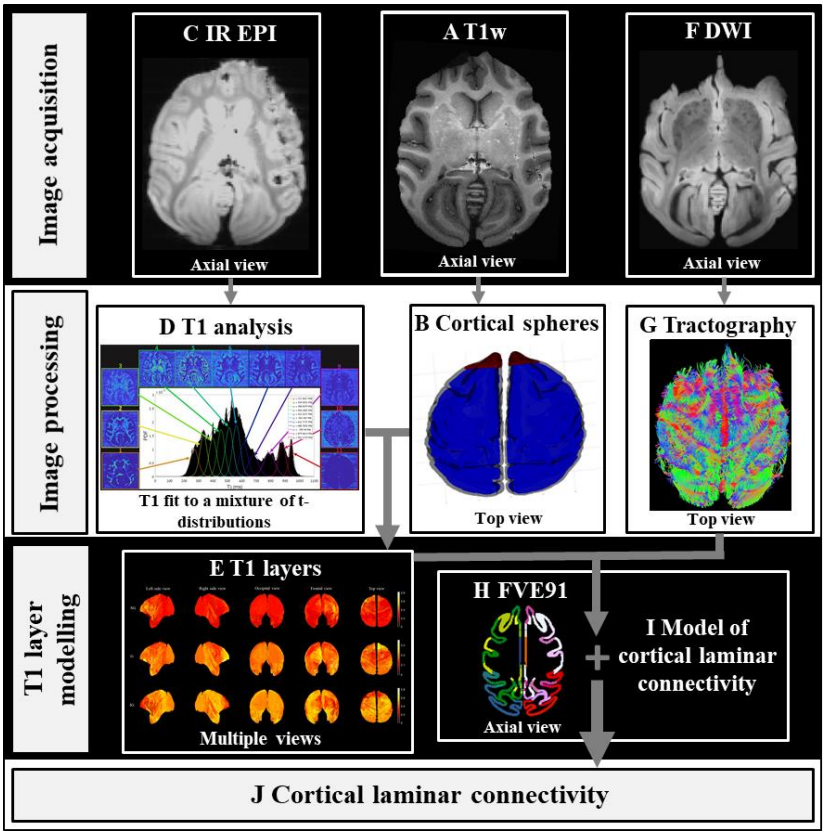

Fig. 3 A streamline summary of our framework for cortical laminar connectivity analysis, including the following steps:

A- T1w image acquisition: anatomical reference;
B- Cortical spheres: sampling volume between delineated cortical surfaces;
C- IR EPI image acquisition: for cortical laminar composition analysis;
D- T1 analysis: mixture model for tissue classification;
E- T1 layers: laminar composition analyzed in spherical sampling system;
F- DWI image acquisition: for global white matter connectivity analysis;
G- Tractography: whole-brain tract analysis;
H- FVE91: all datasets analyzed in atlas space;
I- Model of cortical laminar connectivity: grey and white matter datasets integration;
J- Cortical laminar connectivity: a whole-brain connectome of cortical laminar connections

Results and discussion

This section opens with whole-brain grey matter composition analysis (subsection 1), followed by white matter connectivity analysis: V1 comparison to Felleman and Van Essen's 1991 work as well as whole-brain connectome (subsection 2). The final section starts with the model of cortical laminar connectivity, validated by comparison to Felleman and Van Essen's results, and closes with complex network analysis of the resulting network (subsection 3)

1. T1 layer composition analysis

Following image processing steps 1-4, T1 layers were estimated across the cortical volume. Granular layer 4 (T1 layer 4) was identified according to high probability in V1 and low probability in M1. Since the more myelinated layers lie deeper in the cortex, T1 layers were then easily categorized as supragranular (SG), granular (G) and infragranular (IG) and presented as surface overlays (see figure 4).

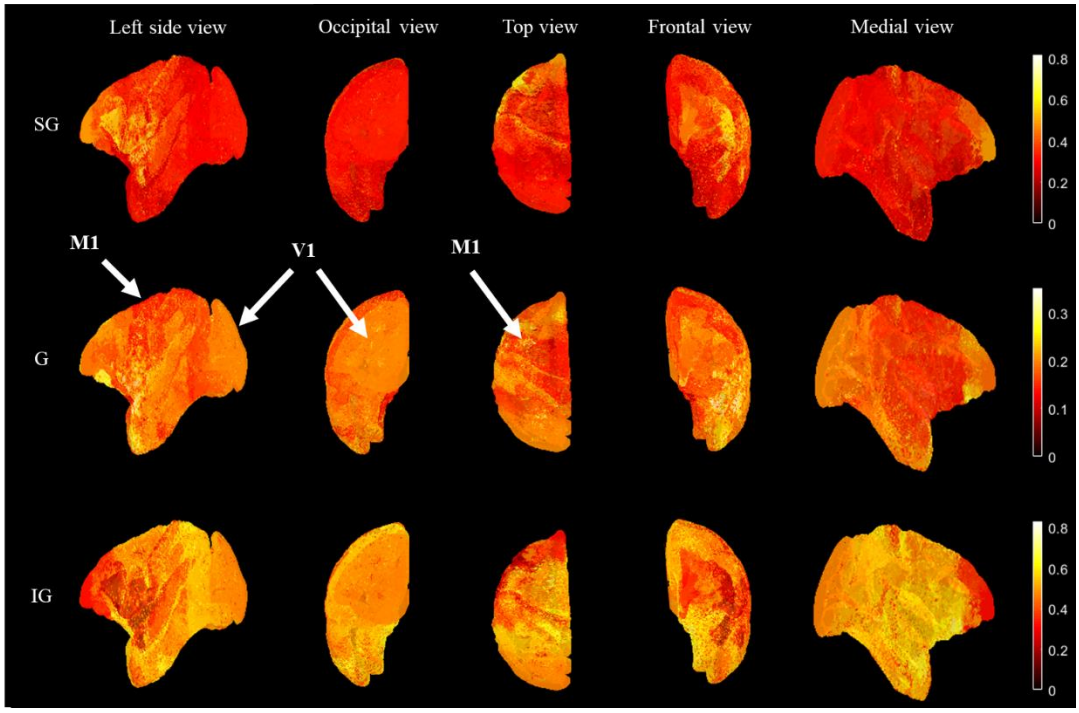

Fig. 4 Macaque cortical laminar probability maps across the left hemisphere:
Top row: supragranular (SG) composition, corresponding to T1 layers 1-3;
Mid row: granular (G) composition, corresponding to T1 layer 4;
Bottom row: infragranular (IG) composition, corresponding to T1 layers 5-6;
Arrows indicate the notable features: low granular presence in the primary visual cortex (V1) and high granular presence in the primary motor cortex (M1)

2. Standard cortical connectivity

2.1 Visual cortex comparison of to Felleman and Van Essen findings

DTI tractography in the visual cortex was compared to Felleman and Van Essen's reported connections between 35 regions of the visual cortex (see figure 5, part 1). Comparison of connectivity matrices demonstrates comparable general patterns of connectivity, with specific regions with higher interconnectedness (V1, V2, V3, Vp, V3A, V4) and others with very sparse interconnectedness (such as CIT and TH). For a dendrogram plot of the hierarchical relationship between clustered regions in the macaque visual cortex, see Supplementary Material figure 5.

In order to quantitatively compare the results in the visual cortex, we binarized both connectivity matrices (see Supplementary Material figure 6). We used Felleman and Van Essen's reported connectivity as the actual results, and our tractography connectivity as the predicted results. Consequently, the accuracy value was estimated at just over 63%.

2.2 Whole-brain cortical connectivity

Whole brain DTI tractography was completed using CSD (constrained spherical deconvolution) across all FVE91 regions. For a full visualization of all model input datasets see figure 5, part 2 (below).

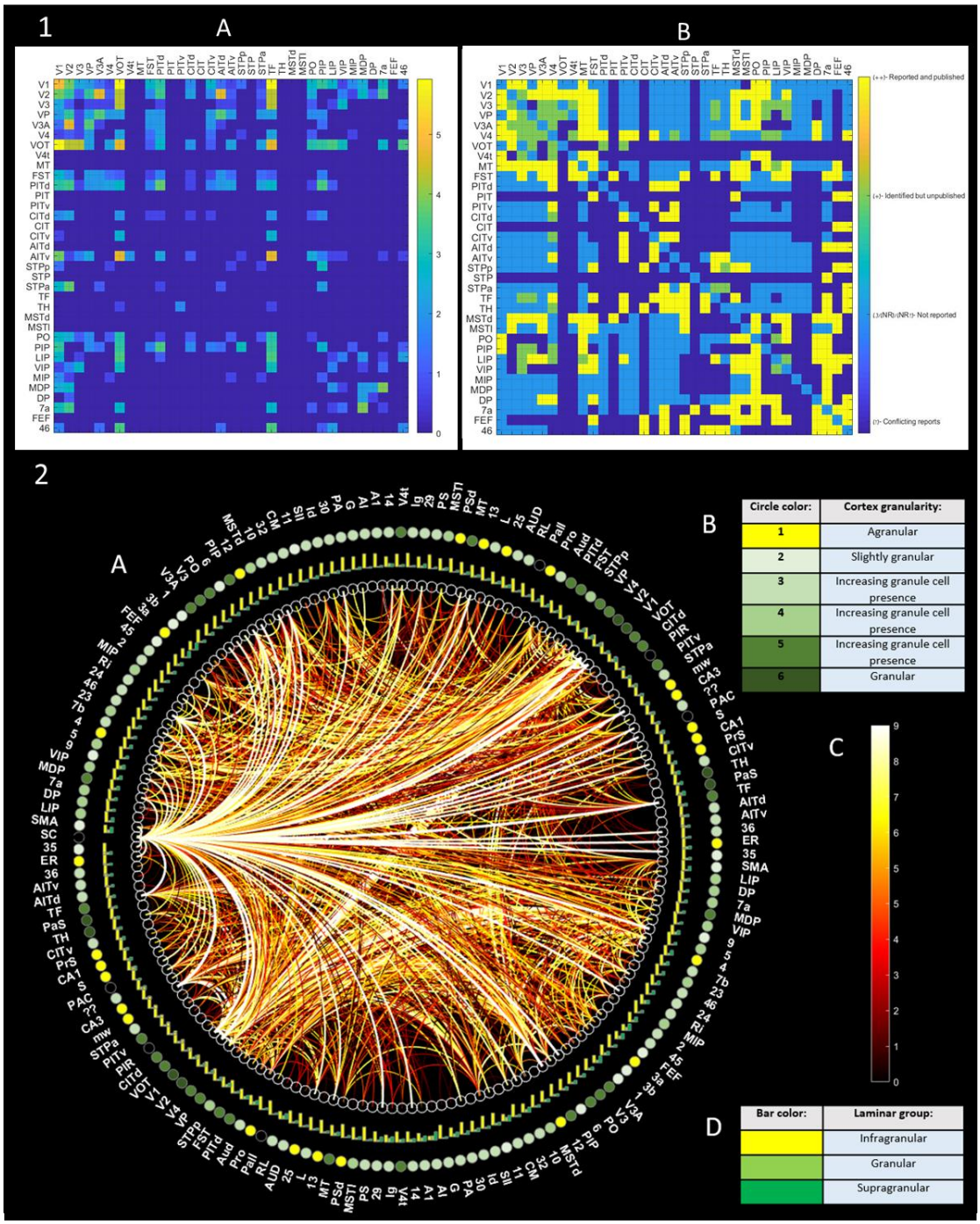

Fig. 5 Macaque cortical connectivity:

Part 1 (top): Macaque visual cortex connectivity:

A- Connectivity matrix, representing log(number of tracts) in visual regions (from tractography)

B- Connectivity matrix of cortical connections reported through tracing (adapted from Felleman and Van Essen 1991)

Part 2 (bottom): A circular network graph of all macaque model input datasets (a), including:

A- Legend for granularity indices, located in the outermost circle;

B- Color scale for global white matter connectomics, representing connection strength of edges;

C- Legend for color bars, representing grey matter laminar composition, located in the first outer circle;

D- K-means clustering of global white matter connectomics, where edges are clustered using k-means based on the connection length and strength and the laminar composition of the connecting regions: cluster histogram (top) and each of the 4 individual clusters (1-4)

(visualized using Circular-Connectome toolbox, available at: github.com/ittais/Circular-Connectome)

3. Cortical laminar connectivity

3.1 Visual cortex comparison of to Felleman and Van Essen findings

Our resulting model of cortical laminar connectivity was compared in the visual cortex to an adaptation of Felleman and Van Essen's reported laminar connections (see figure 6, part 1). Comparison of adjacency matrices demonstrates similarities in unique patterns of connectivity, including generally higher connectedness of infragranular and supragranular laminar compartments, relative to granular connectedness. More specifically, the comparison demonstrates high interconnectedness of supragranular to supragranular compartments and sparse interconnectedness of granular to granular compartments. Results of our model differ from Felleman and Van Essen's in their diagonal connections, as a result of intra-regional vertical connections in our model. These connections are not tractography-based, but rather assumed connections as part of an adaptation of the canonical circuit (Shamir and Assad 2020).

In order to quantitatively compare the results in the visual cortex, once again we binarized both laminar connectivity matrices (see Supplementary Material figure 7). Similarly to section 2.1, we used Felleman and Van Essen's reported laminar connectivity as the actual results, and our resulting model of cortical laminar connectivity as the predicted results. Consequently, the accuracy value was estimated at just over 80%.

3.2 Whole-brain cortical laminar connectivity

We used our unique toolbox for circular connectome visualization in order to display and explore our resulting model of whole-brain laminar connectivity (best viewed online in 3D). Since the resulting network is multilayered, we expanded each regional node into three laminar positions, represented by a different location in the z axis (lowest circle of nodes- infragranular, mid circle of nodes- granular, and highest circle of nodes- supragranular). In addition, because of the multitude of connections and nodes, we also presented intralaminar and interlaminar connections separately (see figure 6, part 2).

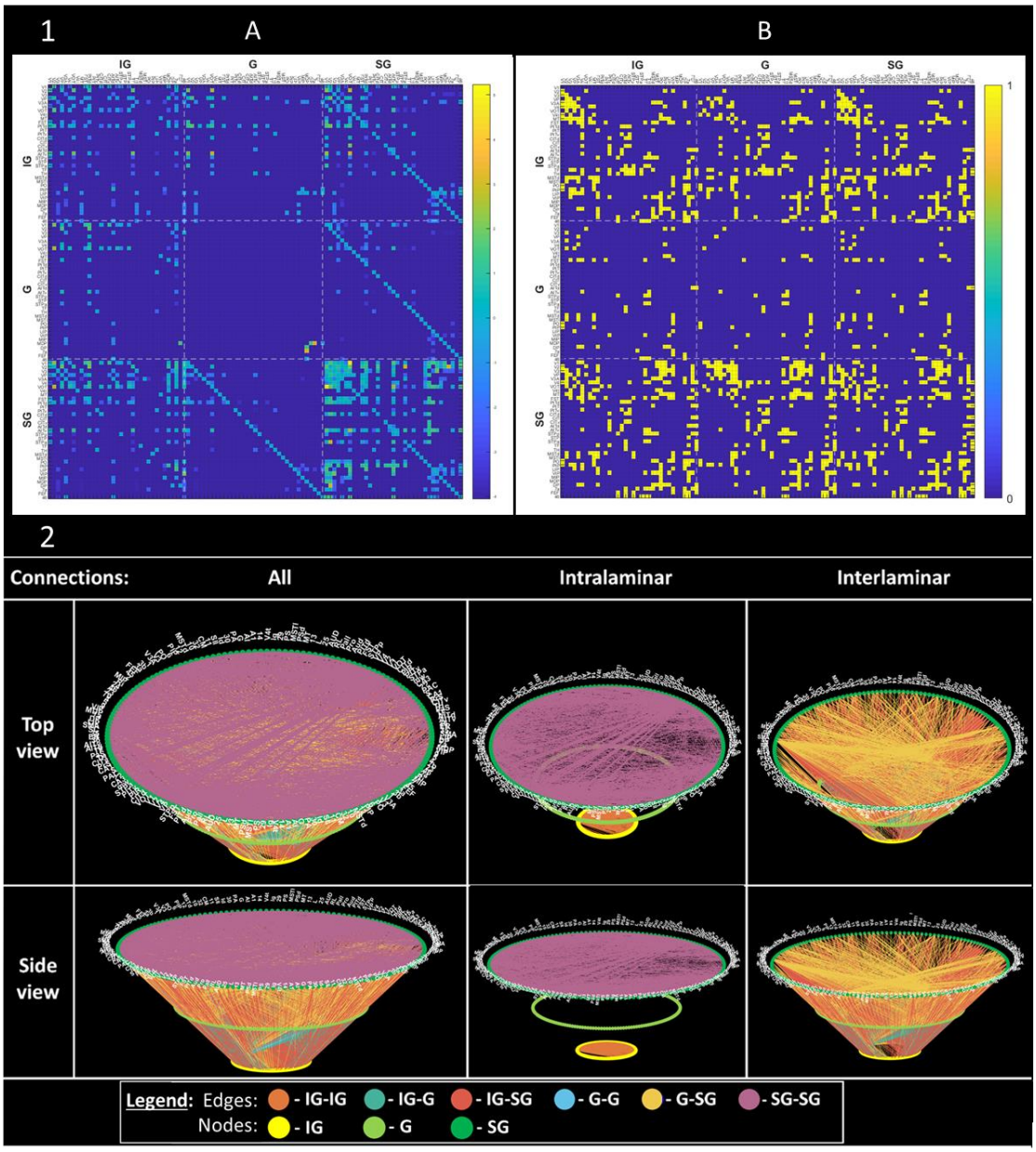

Fig. 6 Macaque laminar connectivity:

Part 1 (top): Macaque visual cortex laminar connectivity:

A- Supra-adjacency matrix, representing laminar-level connections in visual cortex (model results, displayed as log(number of tracts))

B- Supra-adjacency matrix of reported cortical laminar connections, a summarized adaptation of connections reported in (Felleman and Van Essen 1991), according to the following categories:
Origin: supralaminar (S)- SG, bilaminar (B)- IG+SG, infragranular (I)- IG;
Termination: layer 4 (F)- G, columnar (C)- IG+G+SG, multilayer avoiding layer 4 (M)- IG+SG
*If pathway features are reported partially- all laminar categories were marked.

Both matrices include infra-granular (IG), granular (G) and supra-granular (SG) origins and terminations of connections across 35 regions of the macaque visual cortex

Part 2 (bottom): A multilayered circular network graph of macaque cortical laminar connectivity:

Columns: first column represents all model connections, second represents connections within a laminar group, and the third represents connections between laminar groups;

Rows: top row includes a top view of the network graph, while the bottom row includes a side view;

Legend: connections were colored according to connection type, based on the connecting laminar groups (Part 2 is best viewed online in 3D, visualized using Circular-Connectome toolbox, available at: github.com/ittais/Circular-Connectome)

3.3 Complex network analysis

We explored our modelled laminar connectome using complex network analysis tools, similarly to the way in which standard connectomics are explored. In the past, criteria such as rich-club organization (Van den Heuvel and Sporns 2011) and connectivity hubs (Van den Heuvel and Sporns 2013) have been used to gain insight into the organization of the connectome. These criteria and others could easily be adapted and utilized to further explore our modelled laminar connectome.

We chose three straightforward node centrality criteria for exploring both the standard connectome as well as the laminar connectome of the macaque (see figure 13):

1. Node degree signifies the number of edges connected to that node.
2. Node betweenness signifies how often the node appears on a shortest path between two nodes in the network.
3. Nodes closeness signifies the reciprocal of the sum of the length of the shortest paths between the node and all other nodes.

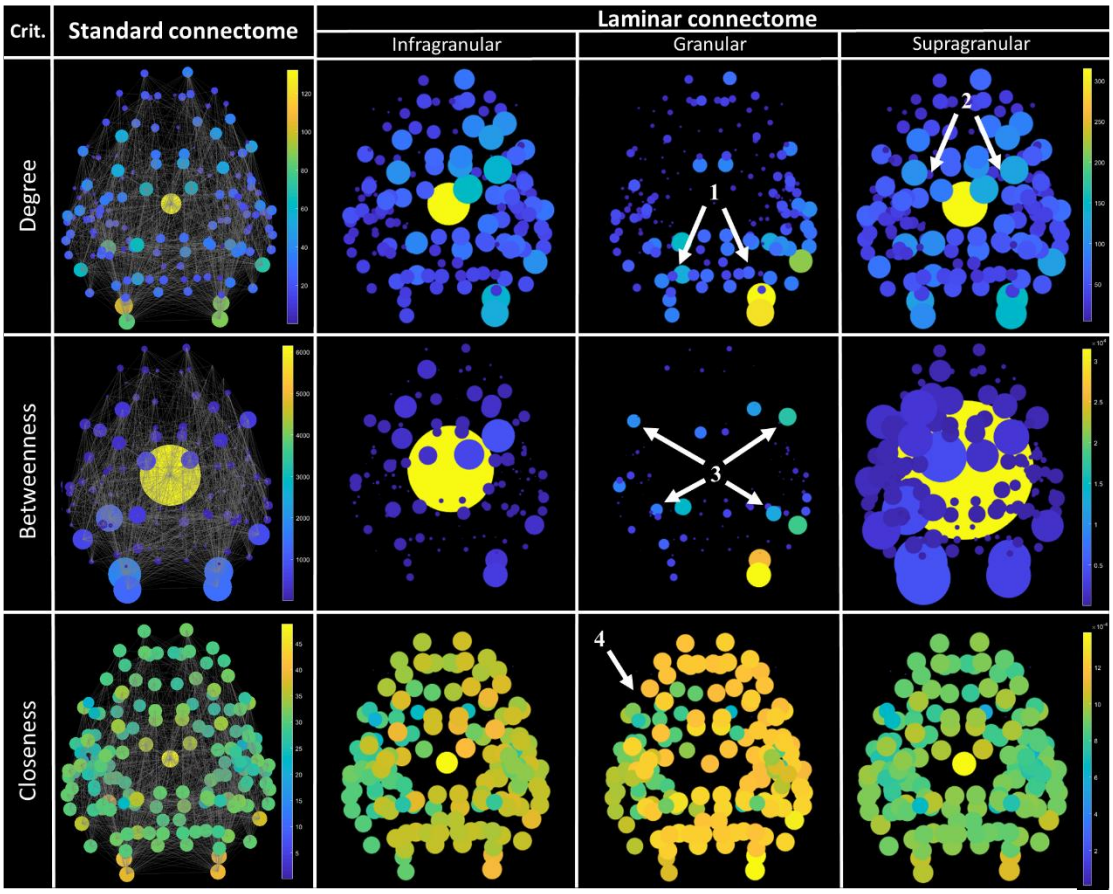

Fig. 7 Comparison of network criteria of standard versus laminar macaque connectomes:
Columns: first column represents standard connectome; second, third and fourth columns represent laminar connectome components (infragranular, granular and supragranular components respectively);
Rows: top row includes node degrees, mid row includes node betweenness and bottom row includes node closeness (all represented across FVE91 regions);
All images from a top view, with node values scaling both circle size and color (legend on right)
Arrows indicate the notable features:
1- High degree values in the granular component in the visual cortex
2- High degree values in the supragranular component in the frontal lobe, around the motor cortex
3- 'Hubs' with high betweenness values in the granular component across both hemispheres
4- Higher closeness values overall in the granular components, relative to the other laminar components

Discussion

In this study, we use multi-modal MRI techniques to model and explore the laminar connectome of the macaque brain. By combining diffusion weighted imaging with T1-weighted imaging and inversion-recovery we were able to implement our data-driven model of cortical laminar connectivity on the macaque brain. This model takes into account not only the white matter interconnections of the cerebral cortex, but also its grey matter heterogenous laminar substructure.

Our choice to focus on the macaque brain was motivated by our desire validate our results in the visual cortex by comparison to Felleman and Van Essen's seminal study about hierarchical processing in the primate visual cortex (Felleman and Van Essen 1991). We recreated the macaque laminar connectivity in the visual cortex and across the entirety of the cortex non-invasively.

On the subject cortical grey matter composition, we used our unique framework for cortical sampling and analysis (Shamir et al. 2019). By implementing this framework for the first time on a nonhuman subject and validating results through granularity-based benchmarks, we gave further validation to the framework and to previous studies on cortical laminar analysis (Barazany and Assaf 2012, Lifshits et al. 2018).

After conducting standard connectivity analysis on the diffusion weighted imaging dataset, white and grey matter datasets were integrated through our novel model of cortical laminar connectivity (Shamir and Assaf 2020). We used our Circular-Connectome toolbox (available at: github.com/ittais/Circular-Connectome) to visualize both the model input datasets as well as the resulting model output in circular graph formats.

In an effort to validate our results, we compared the modelled laminar connectome in the visual cortex to Felleman and Van Essen's widely reported 1991 study on histological tracing results. Their results were adapted and analyzed to match our division of each regional node into three granularity-based laminar components. The comparison included 35 regions across the macaque visual cortex.

The comparison was conducted through visual assessment of the two adjacency matrices, showcasing reported and modelled laminar connections across infragranular, granular and supragranular laminar locations across 35 visual regions. Our results differ from Felleman and Van Essen's specifically in diagonal connections, as a result of intra-regional vertical connections in our model. It is well worth noting that these connections are assumed, rather than tractography-based. They are part of an adaptation of the canonical circuit, which can easily be tweaked and adjusted. Nonetheless, the comparison did demonstrate general similarities in the laminar connectivity patterns. These similarities include generally higher connectedness of infragranular and supragranular laminar compartments, relative to granular connectedness. Another similarity is exhibited in higher laminar interconnectedness within the supragranular laminar compartment, particularly compared to the sparse interconnectedness within the granular compartment. The overall model accuracy in the visual cortex, as compared to Felleman and Van Essen's work, was estimated at around 80%.

The second comparison conducted included the use of network analysis tools to compare the laminar connectome to the standard connectome on which it is partly based. Three centrality criteria were estimated and compared across connectome and laminar components: degree, betweenness and closeness.

Comparison of the degree criterion between the standard and laminar connectomes demonstrates the centrality of the subcortex in the standard connectome as well as the infragranular and supragranular components of the laminar connectome. It appears that the infra- and supragranular layers have a stronger overall contribution to connectedness in the laminar connectome, while in the granular component the occipital lobe and particularly the visual cortex exhibit relatively high centrality and higher degree values. High degree values can also be seen in the supragranular component in the frontal lobe around the motor cortex. Some interhemispheric asymmetry can be seen, specifically in the infragranular and granular components of the laminar connectome.

Comparison of the betweenness criterion between the two connectomes demonstrates the increasing centrality of the subcortex, starting from the standard connectome and progressively in the infragranular and expressly the supragranular connectome. The granular component displays once again high centrality of the visual cortex. Several other betweenness 'hubs' in the granular component also appear in more

frontal regions across both hemispheres. Some interhemispheric asymmetry can be seen across all connectomes and their components.

Comparison of the closeness criterion demonstrates relatively few regional differences within both types of connectome. Nonetheless, there are notable scale differences between the two, where the standard connectome exhibits significantly higher values compared to the laminar connectome. These differences can be explained by the larger number of nodes in the laminar connectome, compared to the standard connectome, resulting in a higher sum of shortest paths to all nodes and a lower resulting value. When comparing individual laminar network criteria, the granular layer demonstrates slightly higher closeness values across the entire cortex.

Conclusions

This study offers a noteworthy application and validation of our proposed novel neuroimaging model of cortical laminar connectivity (Shamir and Assaf 2020). Our MRI-based laminar connectome is compared in the visual cortex to an acclaimed and widescale histological tracing study by Felleman and Van Essen on hierarchical processing in the macaque brain (Felleman and Van Essen 1991). The validity of our model is strengthened by the resulting accuracy level, which was evaluated at a fairly high value of 80%.

We use ex-vivo MRI imaging to recreate and explore laminar level connectivity not only in the visual cortex, but across the entire macaque cortex. By utilizing the progress made in MRI imaging of cortical laminar structure (Barazany and Assaf 2012, Lifshits et al. 2018, Shamir et al. 2019) and integrating it into standard connectomics, we overcome the biased definition of the cortex as one homogenous unit.

Following this validation of our model in the macaque brain, our modelling framework can be used and adapted as needed for implementation in future studies on human subjects. We hope to advance the exploration of connectomics by refining findings from the regional level down to the laminar level. The use of complex network analysis on the laminar connectome will help in refining these observations from standard connectomics and shed more light on why the brain organizes the way it does.

References:

1. Felleman D. J., Van Essen D. C. (1991). *Distributed Hierarchical Processing in the Primate Cerebral Cortex*, Cerebral Cortex, 1, 1-47.
   doi: 10.1093/cercor/1.1.1
2. Van Essen D. C. (2002). *Windows on the brain. The emerging role of atlases and databases in neuroscience*, Current Opinion in Neurobiology, 12: 574-579.
   Doi: 10.1016S0959-4388(02)00361-6.
3. Van Essen D. C., Smith S. M., Barch D. M., Behrens T. E. J., Yacoub E., Ugurbil K.. (2013). *The WU-Minn Human Connectome Project: An Overview*, NeuroImage 80, 62-79.
   doi: 10.1016/j.neuroimage.2013.05.041
4. Setsompop K., Kimmlingen R., Eberlein E., Witzel T., Cohen-Aded J., McNab J. A., Keil B., Tisdall M. D., Hoecht P., Dietz P., Cauley S.F., Tountcheva V., Matschl V., Lenz V. H., Heberlein K., Potthast A., Thein H., Van Horn J., Toga A., Schmitt F., Lehne D., Rosen B. R., Wedeen V., Wald L. L. (2013). *Pushing the limits of in vivo diffusion MRI for the Human Connectome Project*, NeuroImage. 80. 220-233.
   doi: 10.1016/j.neuroimage.2013.05.078
5. Fischl B. (2012). *FreeSurfer*, *Neuroimage*, 62:774–781.
   doi: 10.1016/j.neuroimage.2012.01.021
6. Barazany D., Assaf Y. (2012). *Visualization of Cortical Lamination Patterns with Magnetic Resonance Imaging*, Cerebral Cortex, 22, 2016-2023.
   doi: 10.1093/cercor/bhr277
7. Lifshits S., Tomer O., Shamir I., Barazany D., Tsarfaty G., Rosset S., Assaf Y. (2018). *Resolution considerations in imaging of the cortical layers*, Neuroimage, 164, 112-120.
   doi: 10.1016/j.neuroimage.2017.02.086
8. Shamir I., Tomer O., Baratz Z., Tsarfaty G., Faraggi M., Horowitz A., Assaf Y. (2019). *A framework for cortical laminar composition analysis using low-resolution T1 MRI images*, Brain Structure and Function, vol. 224, is. 4, 1457-1467.

doi: 10.1007/s00429-019-01848-2

9. Peel D., McLachlan G. J. (2000). *Robust mixture modelling using the t distribution*, Statistics and computing, 10(4), 339-348.
   doi: 10.1023/A:1008981510081
10. Shamir I., Assaf Y. (2020). *An MRI-based, data-driven model of cortical laminar connectivity*, medRxiv preprint.
    doi: 10.1101/2020.06.02.20120303.
11. Jbabdi S., Johansen-Berg J. (2011). *Tractography: Where Do We Go from Here?*, Brain Connectivity, Vol. 1, Num. 3, 169-183.
    doi: 10.1089/brain.2011.0033
12. Johansen-Berg H. (2013). *Human connectomics – What will the future demand?*, NeuroImage, 80, 541-544.
    doi: 10.1016/j.neuroimage.2013.05.082
13. Beul S. F., Hilgetag C. C. (2019). *Neuron density fundamentally relates to architecture and connectivity of the primate cerebral cortex*, NeuroImage 189, 777-792.
    doi: 10.1016/j.neuroimage.2019.01.010
14. Tournier J. D., Calamante F., Connelly. A. (2007). *Robust determination of the fibre orientation distribution in diffusion MRI: non-negativity constrained super-resolved spherical deconvolution*, Neuroimage, 35 (2007), 1459–72.
    doi: 10.1016/j.neuroimage.2007.02.016
15. Van den Heuvel M. P., Sporns O. (2011). *Rich-club Organization of the Human Connectome*, Journal of Neuroscience, 31(44), 15775-15786.
    doi: 10.1523/JNEUROSCI.3539-11.2011.
16. Van den Heuvel M. P., Sporns O. (2013). *Network hubs in the human brain*, Trends in Cognitive Sciences, 17(12), 683:696.
    doi: 10.1016/j.tics.2013.09.012